

Gap Plasmon Resonance in a Suspended Plasmonic Nanowire Coupled to a Metallic Substrate

Masashi Miyata,[†] Aaron Holsteen,[‡] Yusuke Nagasaki,[†] Mark L. Brongersma,[‡] and Junichi Takahara^{*,†,§}

[†]Graduate School of Engineering, Osaka University, 2-1 Yamadaoka, Suita, Osaka 565-0871, Japan

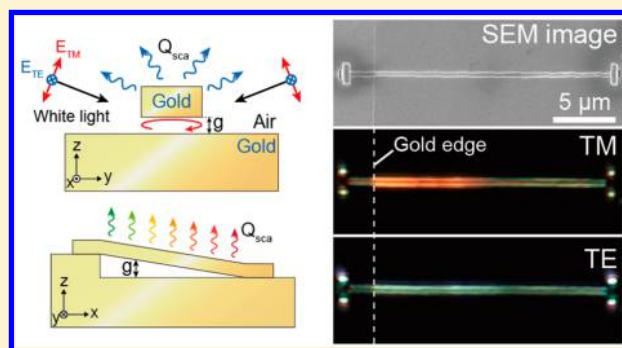
[‡]Geballe Laboratory for Advanced Materials, Stanford University, Stanford, California 94305, United States

[§]Photonics Advanced Research Center, Osaka University, 2-1 Yamadaoka, Suita, Osaka 565-0871, Japan

S Supporting Information

ABSTRACT: We present an experimental demonstration of nanoscale gap plasmon resonators that consist of an individual suspended plasmonic nanowire (NW) over a metallic substrate. Our study demonstrates that the NW supports strong gap plasmon resonances of various gap sizes including single-nanometer-scale gaps. The obtained resonance features agree well with intuitive resonance models for near- and far-field regimes. We also illustrate that our suspended NW geometry is capable of constructing plasmonic coupled systems dominated by quasi-electrostatics.

KEYWORDS: gap plasmon, nanowire, optical antenna, Fabry–Perot resonance, Fano resonance, pick-and-place method



Metallic nanostructures that show collective electronic resonances (surface plasmon resonances) can efficiently confine light into a deep-subwavelength volume, resulting in strong enhancement of electromagnetic fields.^{1,2} Few-nanometer gaps between metals often produce large field enhancements and thus are widely used to design nanostructures for practical applications, such as surface-enhanced spectroscopies^{3–7} and nanophotonics.^{8–11} For the largest field enhancements, it is critical to realize smooth and precisely dimensioned metallic nanogaps to enable strong gap plasmon resonances at a desired wavelength. In recent years, various fabrication approaches such as high-resolution electron beam (EB) lithography,^{3–5} lithography with shadow/angular evaporation,^{6,7} and electromigration,¹² have been used to make metallic nanogaps. Because of the accuracy of these lithographic processes and the surface roughness of deposited metal layers, the quality of the gap plasmon resonances are fundamentally limited. A notable exception is the use of spacing layer to form a metal–insulator–metal (MIM) nanocavity^{13–17} or a film-coupled metallic nanoparticle,^{18–21} which provides a smooth metallic nanogap as well as the precise control of the gap size below 10 nm. However, the spacing layer prevents access to the enhanced field spot (hot spot) in the gap, making them inherently difficult to use in surface-enhanced spectroscopy and in sensing applications, where the resonances are used to enhance light-matter interactions near the surface of the resonator. Because of the current fabrication difficulties and the fundamental geometry limitations, alternative resonator design approaches need to be employed to further explore and utilize the gap plasmon resonances in metallic nanostructures.

Here, we propose and demonstrate the resonator design shown in Figure 1, in which a metallic nanowire (NW) is suspended over a metallic substrate with an air gap. It has been well established that a metallic nanostripe pair with a thin dielectric spacer, such as MIM nanocavities, produces strong resonance modes resulting from the standing-wave of surface plasmons in the gap.^{13,17,22} Because these structures have at least one dimension comparable to the gap plasmon wavelength, their resonant properties are dominated by retardation effects rather than quasi-electrostatics. Therefore, design rules based on radiofrequency antenna design can be applied to such cavities.^{22,23} It is noteworthy that decreasing a gap size of the cavity can lead to extremely large field enhancements in a spacing layer.²¹ In this study, we further develop this resonator concept by forming a suspended NW geometry. As shown in Figure 1a, our structure can locally be viewed as a metallic nanostrip separated with a small gap from a metallic substrate; it can be termed a metal–air–metal (MAM) nanocavity analogous to a MIM nanocavity. As we illustrate later, the NW geometry provides a smooth metallic gap as well as the study of many cavity-gap-sizes even below 10 nm. Also, with our resonator design, there is no material between the NW and the substrate as a spacer so that it can solve the aforementioned problem for MIM nanocavities and film-coupled metallic nanoparticles. This feature also enables us to flexibly change a cavity-gap-size within one fabricated structure by selecting a

Received: June 11, 2015

Revised: July 17, 2015

Published: July 20, 2015

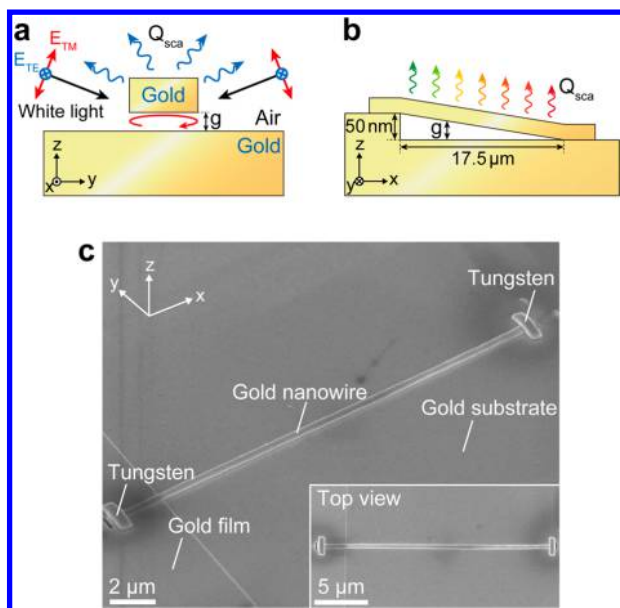


Figure 1. Gap plasmon resonances supported by an individual suspended metal NW. (a,b) Schematic of the cross section (a) and side view (b) of a suspended gold NW above a gold substrate. At various gaps between the NW and the substrate, surface plasmons of different frequencies resonantly oscillate in the gap, which produces strong scattering with various colors. (c) Oblique scanning electron microscopy (SEM) image of a suspended gold NW on a gold substrate. The NW width and thickness are 440 and 80 nm, respectively. Inset shows the top view.

particular location along the NW. In addition to this, suspended MAM structures could be a viable platform to realize tunable gap plasmon resonances when incorporated into nano electromechanical systems (NEMS).^{24,25} An additional appealing feature of this NW is the capability to excite a plasmonic interaction not affected by an adjacent dielectric. Coupled plasmon modes in both classical and quantum regimes are now being extensively studied from the viewpoint of fundamental physics,^{26,27} but they are often disturbed by the impact of surrounding dielectrics (such as a substrate and a spacer).^{27,28} With our present design, we can see the pure near-field response in plasmonic coupled systems, which would provide deep insights into the nature.

In this paper, we first present a fabrication approach based on a probe-based pick-and-place method for constructing a suspended NW geometry that supports metallic nanogaps. With this method, high-quality metallic nanogaps can be realized because of template stripping in the process. We then demonstrate the resonance behavior of the NW by focusing on the scattering property. Spectral analysis and full-field simulation reveal that our structure exhibits strong and clear gap plasmon resonances of various gap sizes down to a single nanometer. We also present the underlying nature of the obtained resonance by applying intuitive resonance models. Finally, we illustrate that our suspended NW geometry is also capable of realizing plasmonic coupled systems dominated by quasi-electrostatics. Our study demonstrates the capability of suspended plasmonic NWs and shows that they act as virtually ideal gap plasmon resonators.

The proposed structure (shown in Figure 1a,b) is fabricated by a pick-and-place method in nanoscale dimensions.^{29,30} The pick-and-place method is based on template stripping with a precisely controlled nanoprobe and has been used to obtain

ultra-smooth metal films with three-dimensional shapes (i.e., bumps, grooves, and apertures).³⁰ However, we now use this method for constructing a suspended NW geometry with a smooth metal-air interface. Figure 2 describes the detail fabrication procedure. First, gold NWs with a width w and a thickness of 80 nm are patterned on a silicon substrate by using EB lithography and a lift-off process. The patterned NW is then stripped with a tungsten probe that is welded to the NW via

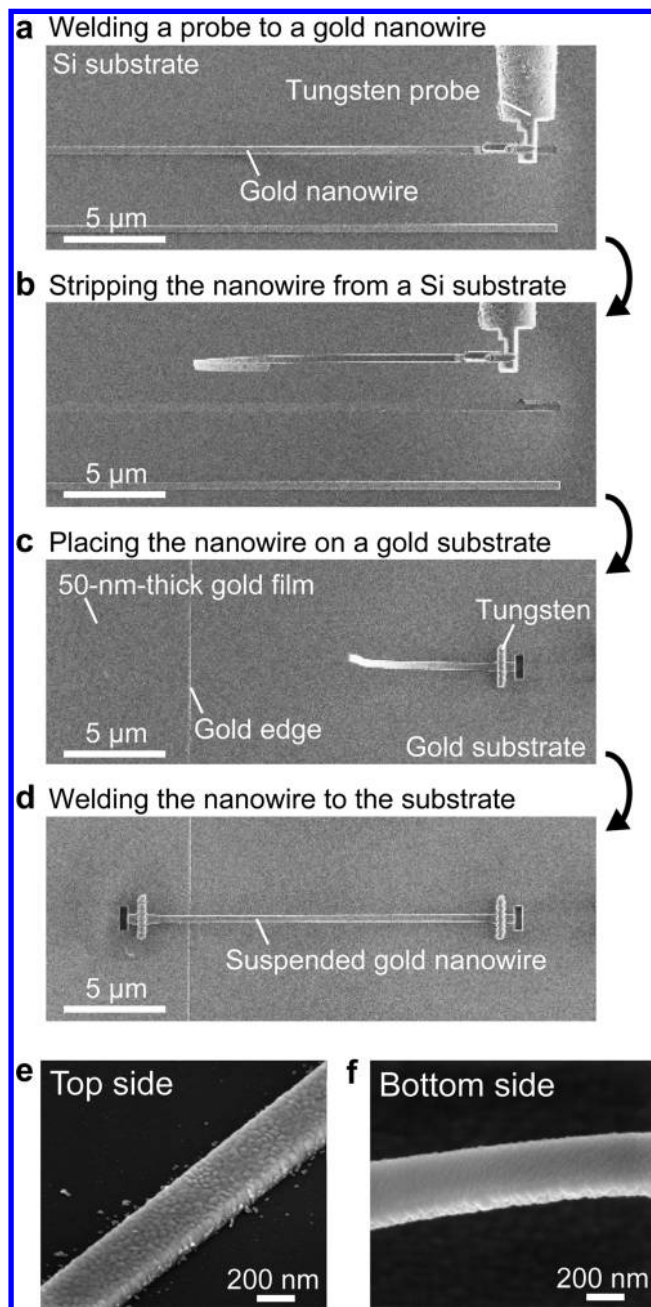


Figure 2. Pick-and-place method for suspended NW fabrication. (a–d) Fabrication procedure. Previously patterned gold NWs on a silicon substrate can be lifted up with a tungsten probe that is welded to the NW by tungsten deposition via focus ion beam (FIB) (a,b). The striped NW is then placed onto a gold substrate and welded to the surface (c). The same procedure is performed to fix the opposite wire-end on a gold film (d). (e,f) SEM images showing the top (e) and bottom (f) side of the NW. The smoothness contrast between the wire top and bottom is obvious.

focused ion beam (FIB) deposition of tungsten (Figure 2a,b). After stripping, the NW is moved onto a gold substrate by the probe and then welded to the substrate surface by tungsten deposition (Figure 2c). The opposite wire end is finally welded to a 50 nm thick gold film to form a suspended NW with a slope, allowing for various gap sizes that include a sub-10 nm gap (Figure 2d). Figure 1c shows scanning electron microscope (SEM) images of a typical fabricated structure ($w = 440$ nm). We also confirmed the quality of the NW surface, presented in Figure 2e,f. As expected, the contrast between the rough (top side, Figure 2e) and the smooth (bottom side, Figure 2f) surfaces is obvious. This will dramatically reduce the impact of surface roughness on the surface plasmons excited in the gap, leading to strong gap plasmon resonances. This feature is the great advantage of the pick-and-place method over previous approaches to realize metallic nanogaps.

To analyze the plasmon resonance properties of the fabricated NW, we measured scattered light under the dark-field white light illumination. The illumination was polarized by a linear polarizer to be in either the transverse magnetic (TM) or transverse electric (TE) polarization defined in Figure 1a. The details of the experimental setup is available in the Supporting Information S1. Figure 3a,b shows dark-field images of the NW with $w = 440$ nm for TM and TE polarized illuminations. We observed that the NW shows various scattering colors that range from red to green along the wire-length-axis under TM illumination, whereas the NW shows only a green color under TE illumination.

Spectral analysis was performed by confocally detecting the scattered light from 16 positions (P_1 – P_{16}) on the NW indicated by white dots in Figure 3a. Figure 3c shows the experimentally observed scattering spectra at each position for TM illumination. From these spectra, we clearly observed resonance peaks and the trend of their red shift in the spectra as the position number increases from P_1 to P_{16} , highlighted by color dots in Figure 3c. As a MAM nanocavity is driven by TM polarized light,^{13,14} these obtained spectral shifts indicate the gap dependence of the plasmon resonances along the width of the NW. We also see weak peaks (blue dots) near the 550 nm wavelength lacking these spectral shifts, indicating gap-independent resonance modes. Spectral analysis for TE illumination was also performed (see Supporting Information S2), in which the spectra show only one peak around 570 nm for all positions with scattering intensities that are roughly three-times less than those of the TM illumination (not shown). In general, TE illumination cannot excite longitudinal plasmon resonance modes, so these weak peaks can be attributed to the intrinsic materials absorption band of gold.

To understand the observed resonant behavior, we evaluated the experimental gap size g by fitting the observed scattering spectra according to full-field simulations. In the suspended NW, it is challenging to accurately measure the gap size by using ordinary measurement methods. In fact, we could not directly measure the gap size values by using atomic force microscopy (AFM) or SEM measurements; AFM measurements changed the structural geometry due to a contact with an AFM tip, and SEM measurements could not provide a clear image of the gap due to the resolution and tilt limitations. Instead, we carried out full-field simulations in order to fit the experimental scattering spectra and estimate the gap size by matching the peak wavelength and amplitude. The full-field simulations were performed with two-dimensional finite element method calculations (COMSOL Multiphysics). For a

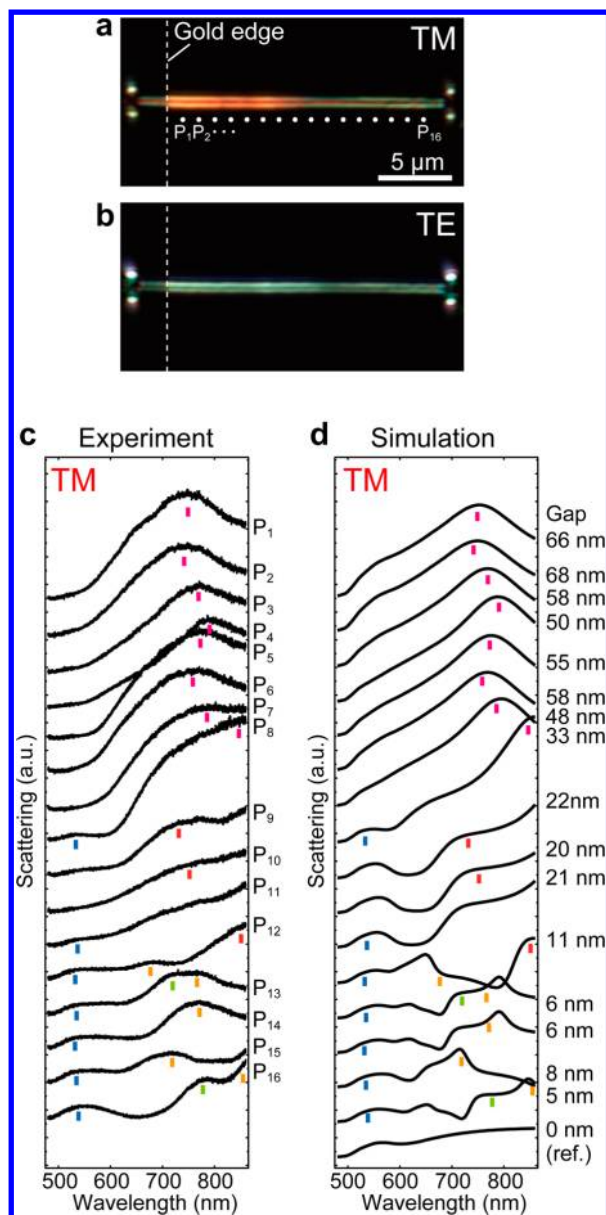


Figure 3. Optical scattering observed from a suspended gold NW on a gold substrate under dark-field white light illumination. (a,b) Dark-field scattering images of a suspended gold NW illuminated by TM (a) and TE (b) polarized light. The vertical dashed white lines represent the gold edge. (c,d) Experimental (c) and simulated (d) scattering spectra for TM polarized illumination. The spectra in experiment were measured at the 16 positions of the NW indicated by the white dots in (a). The gap sizes that were used in the simulation are presented for each simulated spectrum. Color dots in both (c) and (d) show the peak wavelengths extracted from experiments.

better approximation of our measurements, we employed the scattered-field formulation in which the background field is specified using the analytical solution of Fresnel formula for air–gold structure. The scattered field was collected only in the solid angle with $NA = 0.9$ above the NW in a far-field regime, under TM illumination with an incident angle of 72° from the surface normal. In all calculations, we used the dielectric constant of gold obtained by linear interpolation of the experimental data.³¹ The gap separation was the only parameter varied in these simulations.

The calculated scattering spectra of the NW with the fitted gap sizes are presented in Figure 3d. To compare with experiments, the peak wavelengths of experiments are presented by colored dots in each simulated spectrum. As shown, the trend in the experimental spectra, including the spectral shape, peak, and amplitude, is well reproduced by simulations with varying the gap size. Interestingly, the scattering spectra measured at P₁₃–P₁₆ can be well fitted by the simulated spectra with single-nanometer-scale gaps. This clearly indicates that the suspended NW supports a sub-10 nm gap size at P₁₃–P₁₆. We believe that such good agreements with simulations are caused by the high quality of the fabricated gap geometry even in few-nanometer gaps. The fitted gap sizes on all measurement positions are summarized in Figure 4. From this extracted data, it becomes clear that the gap size changes up and down along the NW, covering a gap size of 5–66 nm.

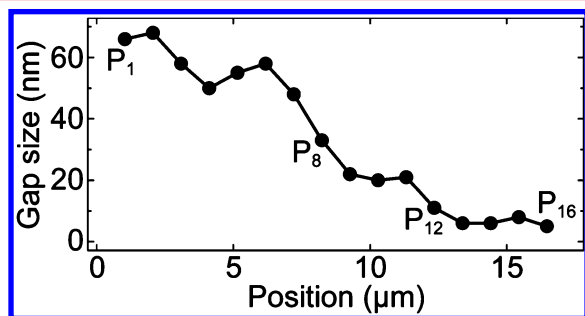


Figure 4. Extracted experimental gap sizes. The gap sizes at 16 measurement positions were extracted by fitting the simulated results to the experimental spectra in Figure 3c.

It is worth noting that the experimental resonance peaks are broadened compared with the simulations. This can be ascribed to the resolution (~ 600 nm) of the confocal setup. Because of the resolution limitation, the experimental spectra present spectral information on scattered light from not only the measurement point but also its vicinity where the resonance peak is slightly red/blue-shifted due to the gap size change along the NW. This directly leads to the broader spectral shape compared with the simulated one. This fact is pronounced on P₈ and P₁₂ where the gap size is rapidly changed (see Figure 4). The dependence on a wire-twist (see Supporting Information S3) as well as the quality of the deposited gold can also be expected to affect the observed spectral shape.

In order to better understand the underlying nature of the observed resonance, we analyzed the electric field distributions at the resonant wavelengths. Figure 5 shows the calculated electric field distributions for the 50 nm gap, 20 nm gap, and 6 nm gap suspended NWs ($w = 440$ nm) with a wavelength of 780, 700, and 780 nm, respectively. From these field maps, it is evident that the NW coupled to the substrate exhibits standing-wave resonances of gap surface plasmons and that the excitation of the resonant modes leads to strong scattering (see Figure 3d). It is also important that our structure shows both odd and even orders of the standing-wave resonance because of the oblique (dark-field) illumination.

To further analyze the resonance features, we performed a large set of simulations similar to those in Figure 3d, which is possible to generate a two-dimensional resonance map for quantifying the predicted resonances as a function of both the wavelength and the gap size, as shown in Figure 6a. Here, we define a scattering efficiency Q_{sc} as the scattering cross section

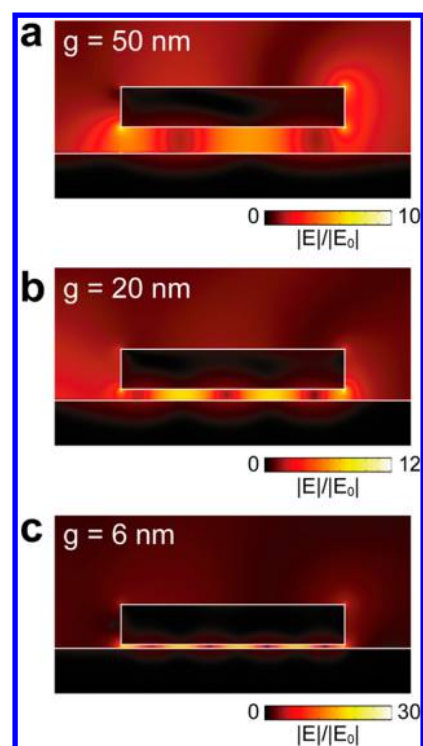


Figure 5. Distributions of the electric field near the NW ($w = 440$ nm) with $g = 50$ nm (a), $g = 20$ nm (b), and $g = 6$ nm (c), illuminated at a wavelength of 780, 700, and 780 nm, respectively. The electric field is normalized to the incident field $|E_0|$.

normalized with respect to the NW width. The map shows multiple peaks and their strong red-shift with decreasing gap size. These resonant behaviors can be understood in terms of an intuitive model of Fabry–Pérot resonances for surface plasmons. Because of the gentle slope of the NW, different cross sections along the NW can locally be viewed as a MAM nanocavity with more or less constant gap. When such a cavity is illuminated by TM polarized light, highly confined surface plasmons are excited in the gap and they resonantly propagate back and forth between the both gap-end-faces at a specific wavelength. This results in a standing-wave of surface plasmons that produces a high field in the vicinity of the both end-faces, contributing to strong scattering. For the standing-wave resonance, the resonant condition is given by the following equation:^{22,23,32,33}

$$\frac{2\pi n_{\text{SPP}}}{\lambda_0} w + \phi = m\pi \quad (1)$$

where λ_0 is the free-space wavelength, n_{SPP} is the effective mode index of the propagating surface plasmons, w is the wire width, ϕ is the phase pickup of the surface plasmons on the end-face reflection, and m is the resonance order. This resonance condition physically corresponds to a situation where the round-trip phase of oscillating surface plasmons perfectly matches with an integer multiple of 2π . To quantify the condition, one needs to investigate the effective mode index n_{SPP} as well as the phase pickup ϕ . These values can be determined according to previously established procedures.²³ In principle, this intuitive model can predict the resonance wavelength and orders on the given structural geometry. The model also indicates that the resonance condition can be tuned by n_{SPP} that is extremely sensitive to the gap size of the cavity.

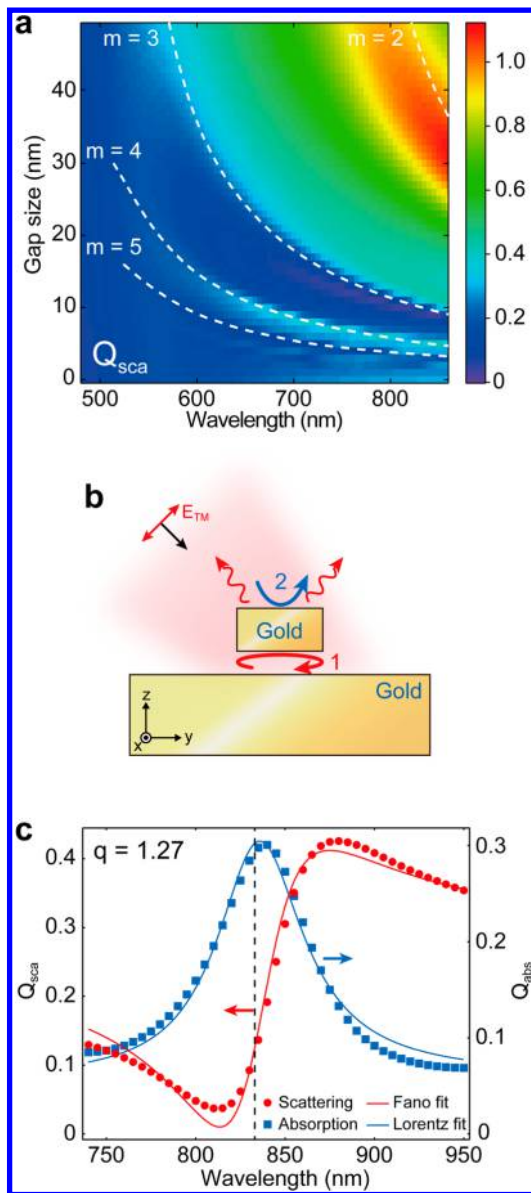


Figure 6. Near- and far-field characterization of the plasmon resonance of the suspended NW. (a) Theoretical resonance map that presents the scattering spectra of the NW at different gaps under the dark-field illumination. Overlaid white lines are the predictions from a Fabry–Pérot model. The resonance orders are indicated for each line. (b) Schematic view of our intuitive understanding of the Fano-type scattering supported by the NW. (c) Calculated scattering and absorption spectra of a 440 nm wide and 10 nm gap suspended gold NW. The red and blue dots show the scattering and absorption efficiency acquired from numerical simulations, respectively. The solid lines show a Fano fit for the scattering spectrum and a Lorentzian fit to the absorption spectrum. The vertical dashed line presents the calculated Fabry–Pérot resonance wavelength.

The white dashed lines in Figure 6a show the obtained resonance condition according to the Fabry–Pérot model. The corresponding orders are indicated with the lines. All calculations were performed by using the simulated values of n_{SPP} and ϕ (see Supporting Information S4). The resonance map shows good agreement with the Fabry–Pérot model for all orders. From the predicted resonance wavelength, we identified the resonance order for each peak in the experiment, illustrating them by the color dots; the pink, red, orange, and yellowish

green dots in Figure 3c correspond to the second-, third-, fourth-, and fifth-order resonances, respectively. The fixed resonance near the 550 nm wavelength (blue dots in Figure 3c) can also be understood by the fact of the Fabry–Pérot resonance on the top face of the NW (see Supporting Information S5).

This well-fitted Fabry–Pérot model aids in understanding the observed spectral behavior. The decrease of the gap size induces a high value of n_{SPP} and it therefore increases the net cavity length for the standing-wave, resulting in the strong red-shift of the resonant wavelength for all resonance orders. The appearance of higher resonance orders especially for gaps of a few nanometers will also be due to the increase of the net cavity length. Likewise, the dependence of the scattering spectra on the wire-twist (see Supporting Information S3) may be explained by the same mechanism. We also investigated the capability of local field enhancements in the NW. The simulations show large field enhancements across the wide spectral range, closely following the Fabry–Pérot model predictions (Supporting Information S6).

It is important to note that the dark-field image of the NW shows a scattering intensity pattern along the wire-length axis. In fact, the image shows the orange/green two-line and the red one-line intensity patterns along the NW (see Figure 3a). This intensity pattern can be explained by the radiation property that is mainly characterized by the resonance order of the Fabry–Pérot resonance. In Supporting Information Section S7, we present the simulated radiation patterns on the NW, which shows the strong dependence on the resonance order that is determined by the gap size. In view of a point spread function at the image plane,³⁴ the simulated results are consistent with the experimentally observed dark-field image.

It is also worth noting that both the experimental and simulated results show an asymmetric spectral shape. This asymmetry can be explained by the occurrence of an optical Fano resonance^{35–37} that results from the interference between the resonantly scattered light through the standing-wave resonance and a nonresonant pathway such as reflected/scattered light by the NW (Figure 6b). The resonant pathway shows a rapidly varying amplitude and phase near the resonance wavelength compared with the nonresonant pathway, so constructive/destructive interference between the two pathways in a far-field regime can give rise to a Fano line shape.

The strength of the Fano-type interference can be modified by the ratio between resonant and nonresonant scattering amplitude; it can be quantified by analyzing the expression for the total scattering efficiency³⁵

$$Q_{\text{sca}}(\omega) \propto \frac{(q\frac{\gamma}{2} + \omega - \omega_0)^2}{(\frac{\gamma}{2})^2 + (\omega - \omega_0)^2} \quad (2)$$

where ω_0 is the resonance frequency, γ is the full-width at half-maximum of the resonance, and q represents the ratio of resonant scattering intensity to the nonresonant scattering intensity. This formula predicts that Fano line shapes are most pronounced when the two scattering pathways are of similar magnitudes ($q \sim 1$). Figure 6c presents the simulated scattering (Q_{sca}) and absorption (Q_{abs} ; total absorption cross section normalized by the NW width) spectra in a 440 nm wide and 10 nm gap suspended gold NW. A fit of eq 2 to the scattering spectrum is also shown in the same figure and yields $q = 1.27$, showing the strong Fano-type interference in a far-field regime.

On the other hand, the simulated absorption spectrum features a Lorentz-type symmetry spectral line and shows the resonance peak identical with the prediction from the Fabry–Pérot model (see the vertical dashed line in Figure 6c). This simply confirms that the absorption is characterized by the near-field energy storage that can be well predicted by the Fabry–Pérot model.

Because of the large NW width ($w = 440$ nm), the suspended NW studied above exhibits high-order resonance modes that are dominated by retardation effects (antenna design rules). In addition to these resonance models, it has been also shown that quasi-electrostatics can account for plasmon resonance behaviors when resonator dimensions are much smaller than the wavelength. In fact, the spectral modification of localized surface plasmon resonances (LSPRs) of metallic nanoparticles coupled to dielectric-coated metallic substrates has been well understood by dipole–dipole interaction in quasi-electrostatics.^{18–21} To study this situation in our suspended NW geometry as well, we explored the resonance behavior of a cylindrical silver NW (with a small diameter) suspended over a gold substrate.

Silver NWs (Sigma-Aldrich, average wire diameter 115 nm) were drop-casted onto a gold substrate with a 50 nm high step to make a suspended NWs (Figure 7a). Here, we focus on an area near a gold edge in which the NW has an air spacer. Figure 7b shows a dark-field image of the NW for TM polarized illumination. We observed a continuous color change from orange to red along the wire-length axis, indicating the gap-dependent resonance behavior. Spectral analysis was performed for this NW by focusing light on six distinct locations along the NW (white dots in Figure 7c). We also simulated the scattering spectra of a 115 nm diameter silver NW with a 10 nm silver sulfide shell ($n_{\text{Ag}_2\text{S}} = 2.9$) by varying the gap size (8 nm step) between the NW and the substrate. The experimental and simulated results are summarized in Figure 7c,d.

Several points should be noted. First, the scattering peaks are slightly red-shifted as the position number increases. Such a spectral change is frequently observed in a metallic nanoparticle–substrate coupled system when a dielectric gap spacer thickness is decreased.^{18–21} As a dipole charge distribution in the metal particle induces an image dipole in the substrate, the decrease of a spatial gap simply increases the dipole–dipole interaction strength and therefore leads to the red-shift of the scattering spectrum. Thus, we interpreted that the measured spectral change will be due to the strength increase by the continuously decreasing gap size along the NW. The simulated results (Figure 7d) also support this expectation. Second, double-peak scattering spectra were observed in P_5 and P_6 where the gap sizes will be smaller than other positions. These double-peak features have been previously reported in a metal nanoparticle coupled to a metal substrate with a dielectric spacer.²⁰ The observed double-peak spectra can be roughly understood by the image dipole approximation (Figure 7e,f). Under dark-field illumination, both the horizontal and the vertical resonance modes of a LSPR can be excited. These two modes will independently interact with their own image dipole in the substrate, resulting in the bonding dipolar plasmon modes. As an electrostatic analysis indicates that the interaction strength with the image dipole for the vertical mode is stronger than that of the horizontal mode, the vertical mode will have a more red-shifted resonance compared with the horizontal mode. Thus, the longer wavelength peaks originate from the vertical mode, whereas the shorter wavelength peaks are

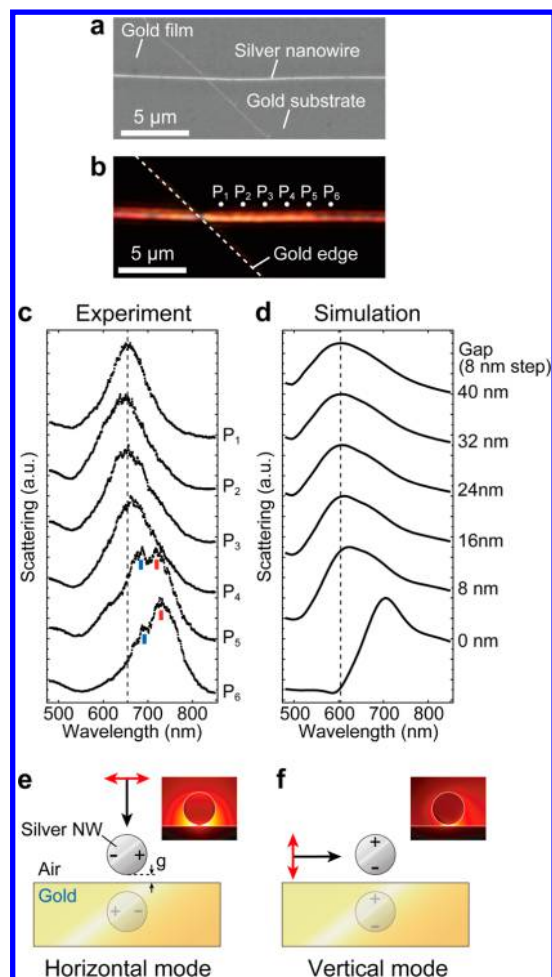


Figure 7. Resonance behavior of a cylindrical silver NW suspended on a gold substrate. (a) SEM image of the NW. The NW diameter is 115 nm. (b) Dark-field image of the NW illuminated by the TM polarization. (c,d) Experimental (c) and simulated (d) scattering spectra for TM polarized illumination. Each spectra in experiment were measured at the six positions indicated by the white dots in (b). The gap sizes that were used in the simulation are presented for each simulated spectrum. The vertical dashed lines show the peak wavelengths of P_1 (for experiment) and $g = 40$ nm (for simulation). All spectral curves are normalized to their maximum value. (e,f) Schematic showing the dipole–dipole interaction for our system. Both the horizontal (e) and the vertical (f) resonance modes can be excited under the oblique illumination. Inset shows the simulated scattered-field distributions under vertical or horizontal illuminations of the 640 nm wavelength.

attributed to the horizontal mode. An additional possible factor of the double-peak spectra is the excitation of a bonding quadrupolar plasmon mode which can be observed for a gap separation $< \sim 2$ nm.^{26,27} As our geometry covers such a nanoscale gap at a particular NW position near a contact point with the substrate, the emergence of the additional bonding mode can also be considered as the reasonable mechanism.

It is important to note that our system does not include a dielectric effect, such as an image dipole inside a dielectric spacer.²⁸ This implies that our measurement shows a pure interaction between LSPRs and a metallic substrate. Furthermore, the suspended NW can potentially realize a nanoscale gap even below 1 nm in which quantum tunneling is expected to play a crucial role.^{27,38} Our geometry may provide an opportunity to experimentally track the gradual

transition from classical ($g > \sim 1$ nm) down to quantum ($g < \sim 1$ nm) regimes within an individual structure. We thus believe that the further experiments for our structure would provide deep insights into the nature of wire/particle–film interactions as well as quantum tunneling in a subnanometer regime.

In conclusion, we have introduced a film-coupled suspended plasmonic NW to construct a smooth metallic nanogap. By employing a nanoscale pick-and-place method, a suspended gold NW on a gold substrate with nanoscale gaps could be successfully fabricated. Our measurements demonstrated that the NW exhibits gap plasmon resonances of various gap sizes even below 10 nm. The obtained spectral features agreed well with intuitive resonance models for near- and far-field regimes, providing clear understanding of the nature of the resonance. Furthermore, we explored a plasmonic coupled system consisting of a cylindrical silver NW suspended over a gold substrate and demonstrated that LSPRs of the NW can be significantly modified via a near-field interaction. We strongly believe that our approach toward the realization of an ideal gap plasmon resonator will be useful in a variety of plasmonic studies and applications where the resonances are used to enhance fields in deep-subwavelength volumes. In particular, enhancing light-matter interactions of nanoscale objects (such as quantum dots and fluorescent molecules) in the air gap is a promising application of our system, which remains for a future study. It is also worth noting that our NW geometry can simultaneously provide various plasmon resonances across a wide range of the visible and near-infrared spectrum within an individual structure. Such tunability could potentially lead to the development of integrated plasmonic chemical and biological sensors. Another potential application based on our resonator would be a NEMS-driven plasmon nanocavity, which remains a tantalizing prospect.

■ ASSOCIATED CONTENT

Supporting Information

Experimental setup details, experimental and simulated scattering spectra under TE illumination, dependence of spectral features on a wire-twist, calculation details of Fabry–Pérot resonance model, simulated results of local enhancement factors, and simulated scattering radiation property. The Supporting Information is available free of charge on the ACS Publications website at DOI: 10.1021/acs.nanolett.5b02307.

■ AUTHOR INFORMATION

Corresponding Author

*E-mail: takahara@ap.eng.osaka-u.ac.jp.

Notes

The authors declare no competing financial interest.

■ ACKNOWLEDGMENTS

We would like to thank Dr. Juhyung Kang and Hamidreza Chalabi (Stanford University) for helpful discussions and technical support on this project. We thank Tatsuya Fujimoto (Osaka University) for his help with fabrication. This work was supported by Grant-in-Aid for Scientific Research B (25286007) from the Ministry of Education, Culture, Sports, Science and Technology, Japan (MEXT). One of the authors (M. Miyata) is supported by Research Fellowships of Japan Society for the Promotion of Science (JSPS) for Young Scientists. The work at Stanford was conducted with Govern-

ment support under and awarded by DoD, Air Force Office of Scientific Research, National Defense Science and Engineering Graduate (NDSEG) Fellowship, 32 CFR 168a, and the U.S. Airforce Office for Scientific Research Grant # FA9550-14-1-0389.

■ REFERENCES

- (1) Mühlischlegel, P.; Eisler, H. J.; Martin, O. J. F.; Hecht, B.; Pohl, D. *W. Science* **2005**, *308*, 1607–1609.
- (2) Schuller, J. A.; Barnard, E. S.; Cai, W.; Jun, Y. C.; White, J. S.; Brongersma, M. L. *Nat. Mater.* **2010**, *9*, 193–204.
- (3) Kinkhabwala, A.; Yu, Z.; Fan, S.; Avlasevich, Y.; Mullen, K.; Moerner, W. E. *Nat. Photonics* **2009**, *3*, 654–657.
- (4) Hatab, N. a.; Hsueh, C.-H.; Gaddis, A. L.; Retterer, S. T.; Li, J.-H.; Eres, G.; Zhang, Z.; Gu, B. *Nano Lett.* **2010**, *10*, 4952–4955.
- (5) Duan, H.; Hu, H.; Kumar, K.; Shen, Z.; Yang, J. K. W. *ACS Nano* **2011**, *5*, 7593–7600.
- (6) Stosch, R.; Yaghobian, F.; Weimann, T.; Brown, R. J. C.; Milton, M. J. T.; Güttler, B. *Nanotechnology* **2011**, *22*, 105303.
- (7) Siegfried, T.; Ekinici, Y.; Martin, O. J. F.; Sigg, H. *Nano Lett.* **2013**, *13*, 5449–5453.
- (8) Dionne, J. A.; Diest, K.; Sweatlock, L. A.; Atwater, H. A. *Nano Lett.* **2009**, *9*, 897–902.
- (9) Atwater, H. A.; Polman, A. *Nat. Mater.* **2010**, *9*, 205–213.
- (10) Choo, H.; Kim, M.; Staffaroni, M.; Seok, T. J.; Bokor, J.; Cabrini, S.; Schuck, P. J.; Wu, M. C.; Yablonovitch, E. *Nat. Photonics* **2012**, *6*, 838–844.
- (11) Moreau, A.; Ciraci, C.; Mock, J. J.; Hill, R. T.; Wang, Q.; Wiley, B. J.; Chilkoti, A.; Smith, D. R. *Nature* **2012**, *492*, 86–89.
- (12) Ward, D. R.; Hüser, F.; Pauly, F.; Cuevas, J. C.; Natelson, D. *Nat. Nanotechnol.* **2010**, *5*, 732–736.
- (13) Miyazaki, H. T.; Kurokawa, Y. *Phys. Rev. Lett.* **2006**, *96*, 097401.
- (14) Miyazaki, H. T.; Kurokawa, Y. *Appl. Phys. Lett.* **2006**, *89*, 211126–211126.
- (15) Jung, J.; Sondergaard, T.; Bozhevolnyi, S. I. *Phys. Rev. B: Condens. Matter Mater. Phys.* **2009**, *79*, 035401.
- (16) Chandran, A.; Barnard, E. S.; White, J. S.; Brongersma, M. L. *Phys. Rev. B: Condens. Matter Mater. Phys.* **2012**, *85*, 085416.
- (17) Lassiter, J. B.; McGuire, F.; Mock, J. J.; Ciraci, C.; Hill, R. T.; Wiley, B. J.; Chilkoti, A.; Smith, D. R. *Nano Lett.* **2013**, *13*, 5866–5872.
- (18) Holland, W. R.; Hall, D. G. *Phys. Rev. Lett.* **1984**, *52*, 1041–1044.
- (19) Mock, J. J.; Hill, R. T.; Degiron, A.; Zauscher, S.; Chilkoti, A.; Smith, D. R. *Nano Lett.* **2008**, *8*, 2245–2252.
- (20) Hu, M.; Ghoshal, A.; Marquez, M.; Kik, P. G. *J. Phys. Chem. C* **2010**, *114*, 7509–7514.
- (21) Ciraci, C.; Hill, R. T.; Mock, J. J.; Urzhumov, Y.; Fernandez-Dominguez, A. L.; Maier, S. A.; Pendry, J. B.; Chilkoti, A.; Smith, D. R. *Science* **2012**, *337*, 1072–1074.
- (22) Bozhevolnyi, S. I.; Sondergaard, T. *Opt. Express* **2007**, *15*, 10869–10877.
- (23) Barnard, E. S.; White, J. S.; Chandran, A.; Brongersma, M. L. *Opt. Express* **2008**, *16*, 16529–16537.
- (24) Craighead, H. *Science* **2000**, *290*, 1532–1536.
- (25) Kim, J.-H.; Chen, Z. C. Y.; Kwon, S.; Xiang, J. *Nano Lett.* **2014**, *14*, 1687–1691.
- (26) Romero, I.; Aizpurua, J.; Bryant, G. W.; García De Abajo, F. J. *Opt. Express* **2006**, *14*, 9988–9999.
- (27) Scholl, J. A.; García-Etxarri, A.; Koh, A. L.; Dionne, J. A. *Nano Lett.* **2013**, *13*, 564–569.
- (28) Knight, M. W.; Wu, Y.; Lassiter, J. B.; Nordlander, P.; Halas, N. J. *Nano Lett.* **2009**, *9*, 2188–2192.
- (29) Nagpal, P.; Lindquist, N. C.; Oh, S. H.; Norris, D. J. *Science* **2009**, *325*, 594–597.
- (30) Lindquist, N. C.; Johnson, T. W.; Norris, D. J.; Oh, S. H. *Nano Lett.* **2011**, *11*, 3526–3530.
- (31) Johnson, P. B.; Christy, R. W. *Phys. Rev. B* **1972**, *6*, 4370–4379.

- (32) Novotny, L. *Phys. Rev. Lett.* **2007**, *98*, 266802.
- (33) Barnard, E. S.; Pala, R. A.; Brongersma, M. L. *Nat. Nanotechnol.* **2011**, *6*, 588–593.
- (34) Novotny, L.; Hecht, B. *Principles of Nano-Optics*; Cambridge University Press: Cambridge, U.K., 2006.
- (35) Fano, U. *Phys. Rev.* **1961**, *124*, 1866–1878.
- (36) Luk'yanchuk, B.; Zheludev, N. I.; Maier, S. A.; Halas, N. J.; Nordlander, P.; Giessen, H.; Chong, C. T. *Nat. Mater.* **2010**, *9*, 707–715.
- (37) Fan, P.; Yu, Z.; Fan, S.; Brongersma, M. L. *Nat. Mater.* **2014**, *13*, 471–475.
- (38) Savage, K. J.; Hawkeye, M. M.; Esteban, R.; Borisov, A. G.; Aizpurua, J.; Baumberg, J. J. *Nature* **2012**, *491*, 574–577.